Research Square

Preprints are preliminary reports that have not undergone peer review.
They should not be considered conclusive, used to inform clinical practice,
or referenced by the media as validated information.

Dynamic crop-atmosphere water feedbacks challenge isotopic equilibrium knowledge in the lower atmospheric boundary layer

Adrian Dahlmann

adrian.dahlmann@zalf.de

Leibniz Centre for Agricultural Landscape Research (ZALF) https://orcid.org/0000-0001-8195-5375

David Dubbert

Leibniz Centre for Agricultural Landscape Research (ZALF)

Mathias Hoffmann

Leibniz Centre for Agricultural Landscape Research (ZALF) https://orcid.org/0000-0002-2776-1403

John Marshall

University of Gothenburg

Gunnar Lischeid

Leibniz Centre for Agricultural Landscape Research

Maren Dubbert

Zalf https://orcid.org/0000-0002-2352-8516

Article

Keywords:

Posted Date: April 3rd, 2026

DOI: https://doi.org/10.21203/rs.3.rs-9103465/v1

License: This work is licensed under a Creative Commons Attribution 4.0 International License.
Read Full License

Additional Declarations: There is **NO** Competing Interest.

Dynamic crop-atmosphere water feedbacks challenge isotopic equilibrium knowledge in the lower atmospheric boundary layer

*Adrian Dahlmann[1,2,4], David Dubbert[1], Mathias Hoffmann[1], John Marshall[1,3], Gunnar Lischeid[1,2] and Maren Dubbert[1,4]

[1] Ecophysiology of Water and Matter Cycling, Leibniz Centre for Agricultural Landscape Research (ZALF), 15374 Müncheberg, Germany
[2] Institute of Earth and Environmental Sciences, University of Potsdam, 14476 Potsdam, Germany
[3] Department of Earth Sciences, University of Gothenburg, Gothenburg, 405 30, Sweden
[4] Institute of Crop Science and Resource Conservation, University of Bonn, 53115 Bonn, Germany

Abstract

Understanding water fluxes in agricultural ecosystems is fundamental to securing food production under increasing water scarcity. This study investigates the dynamics of evapotranspiration (ET) and its stable water isotopic composition ($\delta^{18}O$, $\delta^{2}H$) in a heterogeneous cropland cultivated with winter oil rapeseed and winter wheat. By coupling a fully automated chamber system with high-resolution in-situ laser spectroscopy, we implemented a novel observational approach that achieved the continuous monitoring of ambient water vapor, precipitation, and ET isotopic compositions at an unprecedented temporal resolution over two growing seasons.

We found the isotopic composition of ET to serve as a sensitive indicator of crop phenology and physiological response to changing environmental conditions and observed a distinct seasonal shift from evaporation-dominated to transpiration-dominated fluxes. High transpiration rates strongly affected the ambient water vapor diurnally and seasonally, challenging common ecohydrological assumptions. Furthermore, we demonstrate that a data-driven Random Forest model can successfully predict the complex, non-linear dynamics of isotopic compositions using standard micrometeorological variables and easily measurable ambient water vapor compositions. We conclude that high-resolution monitoring linked with machine learning offers a robust pathway to disentangle spatio-temporal dynamics of soil-plant-atmosphere interactions and improves our ability to predict crop water dynamics under changing environmental conditions.

1. Introduction

Evapotranspiration (ET), the combined process by which water moves from the land surface to the atmosphere through soil evaporation, plant transpiration and interception, is a key component of the water cycle of agroecosystems[1]. In regions facing water scarcity, quantifying ET is essential for managing water resources sustainably and predicting how ecosystems will respond to changing climatic conditions[2].

Methods for quantifying ET have evolved from plot-scale lysimeters[3] to landscape-scale eddy covariance systems[4]. To simplify plot-scale measurements, gas-exchange chambers complement these approaches[5]. Initially, labor-intensive manual chamber systems dominated research, offering limited temporal and spatial resolution[5]. Specifically, the transition to automated chamber systems has resolved previous limitations by enabling continuous, high-frequency measurements with minimal disturbance[6]. These fully automated chamber systems allow to capture both spatial variabilities, such as soil heterogeneity, and temporal dynamics, including responses to precipitation and crop phenology across multiple seasons. This is particularly relevant in landscapes where e.g., soil erosion has created distinct gradients in hydraulic properties and water storage capacities- factors which directly influence plant water availability and drought susceptibility at the a small-scale[7]. This is furthermore strongly modulated by seasonality and weather extremes, such as drought, which can decouple evaporation and transpiration fluxes and alter stomatal regulation[8]. To trace these soil- and plant-dependent impacts on ET, which results in phytoclimatic changes under varying climatic stress, high-resolution monitoring is essential.

Beyond flux quantification, analyzing stable water isotopes ($\delta^{18}O$ and $\delta^{2}H$) has become a powerful method for tracing and interpreting water movement, particularly in agricultural landscapes[9]. The basis for isotopic investigations was initially laid by discrete destructive sampling of soil or plant material, followed by water extraction and laboratory analysis[10]. The introduction and widespread adoption of laser-based absorption spectroscopy like cavity ring-down spectroscopy (CRDS) have revolutionized our ability to make continuous in situ measurements of water vapor concentration and isotopic composition with high accuracy and temporal resolution[11–22]. These high resolution measurements have been used to investigate the soil-plant-atmosphere continuum (SPAC) in ecohydrology[11] with studies about root-water-uptake and xylem transport[18,19,23], partitioning of ET[11,21,24], and atmospheric processes [23,25,26].

They have also been used to calibrate and validate process based ecohydrological models like the EcH2O-iso, which can be used to model water ages and travel time distribution[23,27]. Especially for ET partitioning, various methods are based on stable water isotopes, e.g. the Keeling-Plot-Method, the Flux-Gradient-Method, EC with isotopes and open or closed chamber methods[13,21,28,29]. Although these approaches are improving rapidly, they are still based on major assumptions that lead to uncertainties. For example, many EC partitioning approaches assume that ecosystem ET is predominantly driven by T (ET = T) under ideal transpiring conditions, specifically that the transpired water is in an isotopic-steady-state (ISS) with the xylem water (δ_A). However, we already know this is not the case for every ecosystem[12,30]. In addition, many studies assume that atmospheric water vapor is in equilibrium with current or recent rainfall [10,20,21,31]. This simplifying assumption has also been questioned recently[15,23]. Although the breakdown of these simplifying assumption complicates ET modelling, understanding these complex interactions within the SPAC across spatial and temporal scales is fundamental to our understanding of the water cycle of terrestrial ecosystems [32]. Particularly in agriculture, tracking the diurnal and seasonal dynamics of stable water isotopes across the soil-plant-atmosphere continuum is essential for quantifying exact water use. By resolving the specific ratio of beneficial transpiration to evaporative loss, these high-resolution insights allow for the optimization of irrigation schedules and land-use strategies. Such precision management is vital for securing water resources, thereby mitigating stakeholder conflicts and preventing economic losses at the landscape scale[7,20,21].

Our research seeks to contribute to this integrated understanding by investigating the agricultural water cycle in one of Germany's driest regions, focusing specifically on SPAC interactions under increasingly extreme environmental conditions due to climate change. We are employing a fully automated closed chamber system to continuously measure ET. This system is combined with in-situ stable water isotope measurements ($\delta^{18}O$ and $\delta^{2}H$ in water vapor), enabling us to determine the isotopic signature of the ambient water vapor (δ_A) within the lower atmospheric boundary layer and, ET (δ_{ET}) using the Keeling Plot approach [21,33]. Using these methods, we examine the connections between the isotopic composition of ET (δ_{ET}), precipitation (δ_{Pr}) and ambient water vapor (δ_A) under changing environmental conditions on a diurnal to seasonal scale. We hypothesize that:

- Small-scale soil heterogeneity, plant phenology, and weather extremes (e.g., drought events) shape ET and ambient water vapor dynamics.
- In turn, spatio-temporal dynamics of ET modify the isotopic composition of ambient water vapor, which feeds back on the atmospheric equilibrium with precipitation.

To date, modelling of stable water isotopes in ecohydrology has predominantly relied on physically based approaches. These range from analytical formulations describing fractionation during phase changes, such as the Craig–Gordon model for soil evaporation and non-steady-state models for leaf water enrichment[34,35], to complex, distributed ecohydrological models, such as EcH$_2$O-ISO, SiSPAT-Isotope, and Soil-Litter-ISO[27,36,37]. While effective, they often require extensive parameterization, rely on simplified mixing assumptions, and demand substantial computing power[11,38]. In addition, using any kind of measurement system inevitably results in data sets with gaps. Previously, data-driven machine learning (ML) approaches have been successfully established for scaling up and filling in gaps in water and carbon flux data [7,39]. Here, we combined for the first time easily measured, high-resolution δ_A data, modern machine learning methods, and self-organizing maps with Sammon's mapping (SOM-SM) to explore a simpler method of predicting δ_{ET}. Our multifaceted approach aims to provide insights into how the agricultural system responds to climatic stress and the linkages between the land surface and the ambient water vapor. This will become increasingly important in light of conflicts over water use.

2. Results

2.1 Environmental conditions and plant specific parameters

The photosynthetic active radiation (PAR) well reflects the seasonal variation of the day length, with reduced values during periods of high cloud cover (Fig. 1). From the beginning of September to the end of August during the 2021/22 and 2022/23 cultivation periods, the mean temperature was 10.5 and 10.1 °C, respectively, and total precipitation was 363 and 376 mm, respectively. These cultivated seasons were significantly drier and warmer compared to the previous 30 seasons from September 1991 to August 2021 with an average of 497 mm

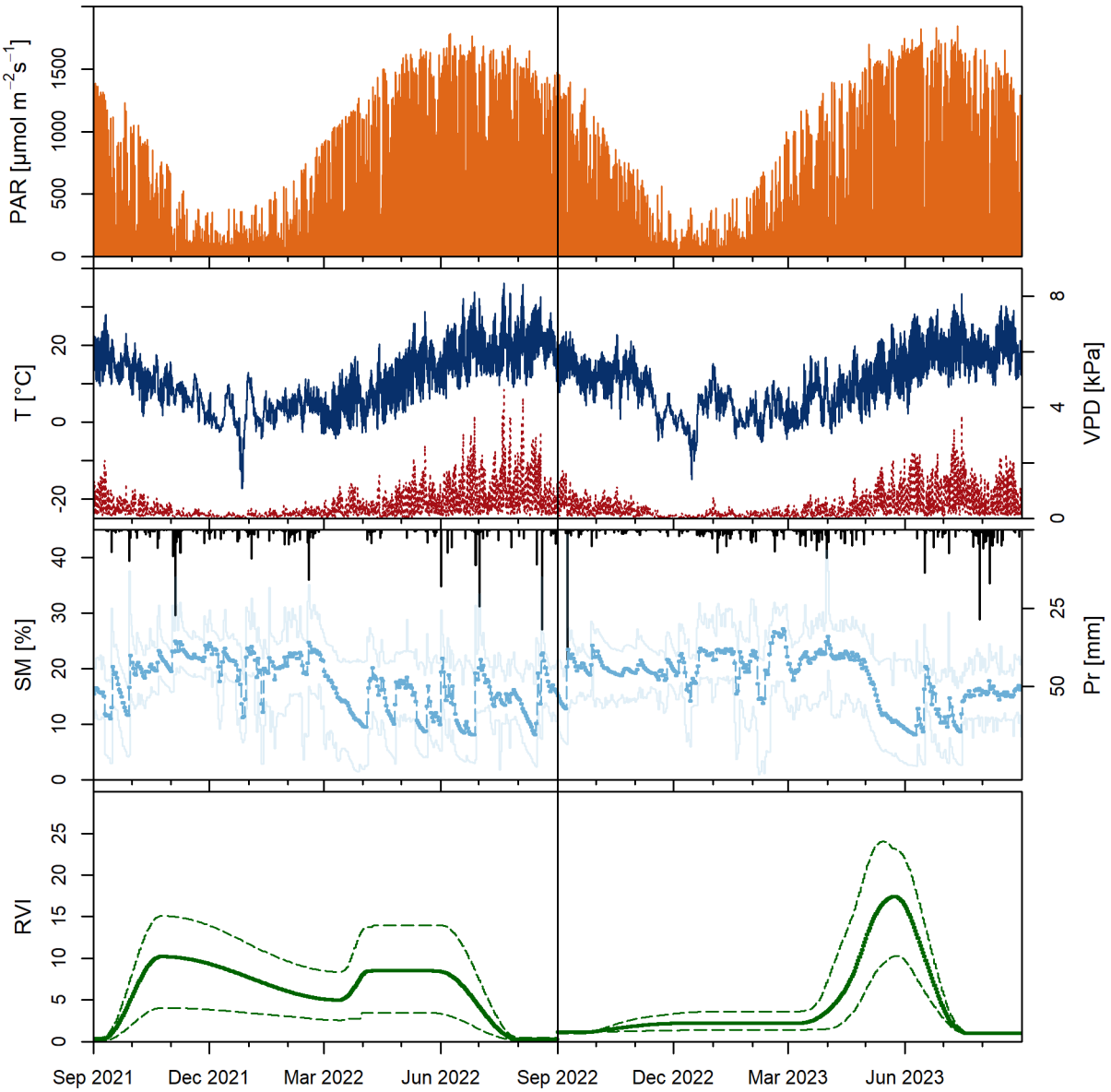


Fig. 1: Time series of environmental and plant-growth parameters. The panels show (from top to bottom): (1) Photosynthetically active radiation (PAR; orange); (2) air temperature (T; blue) and vapor pressure deficit (VPD; red); (3) soil moisture (SM; blue line) with precipitation (bars); and (4) the Ratio Vegetation Index (RVI; green). In panel 3 and 4, the light blue shaded lines and dashed lines represent the minimum to maximum variation across the plots.

precipitation and a mean seasonal temperature of 8.9°C (ZALF weather station in Dedelow, Germany, located ~1 km away). There are two noticeable dry periods without precipitation events, one of 37 days starting 2022, February 26th and the other of 17 days starting 2023, May 24th. Here, the soil moisture in 5 cm depth was clearly connected to precipitation events and plant water use, particularly during periods of drought, such as March 2022, and periods of high plant activity, such as June 2023. Linked to the dry period starting in May 2023, there was a soil moisture decrease over 40 days from May 1st to June 9th, 2023, with only 3.9 mm precipitation (three events) resulting in a lack of plant available water during the main growing period. The decrease in soil moisture was visible down to 45 cm and less pronounced for the non-eroded soil. The RVI exhibits the typical growth pattern of the cultivated plants. For rapeseed, a rapid increase is visible due to high soil coverage already starting from fall 2021 followed by a loss in plant material in winter. Starting in spring 2022, there is a second rapid increase in RVI to a plateau due to the loss of leaves which is compensated through pod growth. The comparison with the second year of winter wheat reveals a contrasting pattern, with minimal growth in the fall of 2022, followed by accelerated growth in the spring of 2023 and a subsequent rapid decline due to ripening.

The soil water potential (SWP) at different depths was used to identify periods of plant stress due to drought (Fig. 2). During summer, SWP reveals clear periods without plant available water (<-15 MPa) in the upper 45 cm in the extremely eroded soil type (eE) and less negative values for both the strongly eroded soil (sE) and non-eroded soil (nE). At 45 cm depth, soil

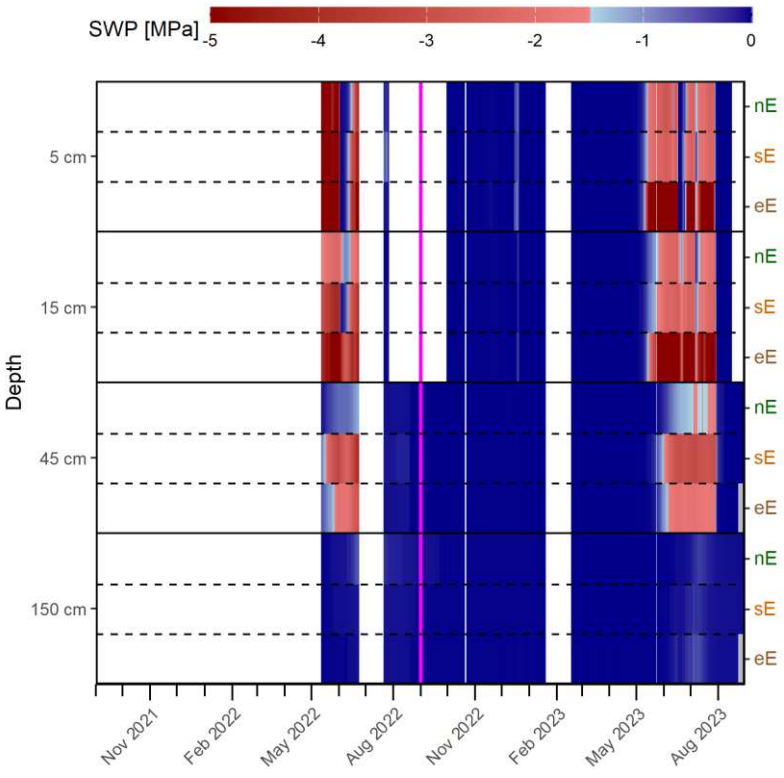


Fig. 2: Soil water potential over the observation period. Four different depth (5, 15, 45 and 150 cm) and three soil types (non-eroded LV-cc = nE, strongly eroded LV-ng = sE and extremely eroded RG-ca = eE; see labels on right axis). Vertical magenta line indicates the change of seasons. Data gaps (white) originate from deinstallation during tillage and sensor failures. Values between -5 and -15 MPa are summarized for a better visibility.

available water decreases only during the main growing periods and predominantly for eroded soils (sE and eE) while nearly no changes are recorded in 150 cm depth.

2.2 ET fluxes

Data-driven modeling using the random forest (RF) approach yielded good to very good results in predicting ET fluxes (classification according to Dahlmann *et al.*[7]), revealing the seasonal variability driven by changing plant activity and environmental parameters (3 a). As expected,

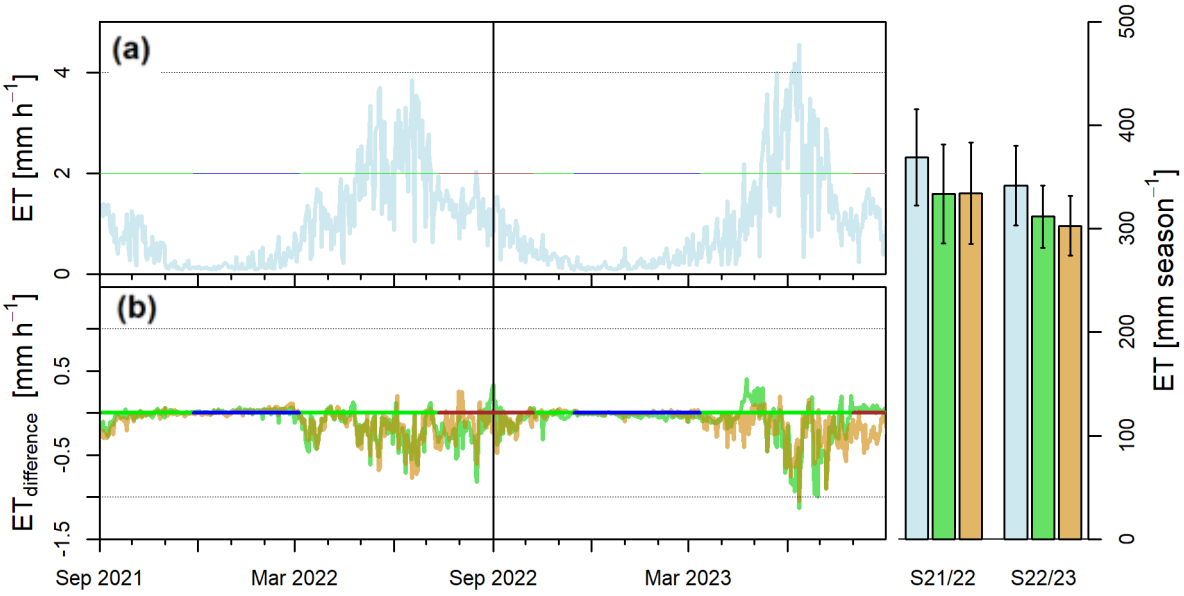


Fig. 3: ET fluxes from two-seasons, noting the cultivation cycles of rapeseed (S21/22) and winter wheat (S22/23). The upper panel shows the ET fluxes for the non-eroded LV-cc (nE; light blue), the lower the ET flux differences of strongly eroded LV-ng (sE; green) and extremely eroded RG-ca (eE; brown) to LV-cc. Vertical lines indicate the change of seasons and color of the x-axis denotes different periods during the year with: green for growth, brown for fallow land, and blue for winter dormancy. In the right panel, the mean seasonal balances with standard deviation are shown.

low ET fluxes were found during the non-growing periods in winter (blue horizontal line), while rising ET values were found during growth (green horizontal line) following the increasing plant growth. For the oil rapeseed growing season, the ET started to increase earlier, compared to the winter wheat growing season, but displaying lower maximum fluxes. During the fallow period after harvest (brown horizontal line), ET was dominated by soil evaporation driven by available soil water and environmental conditions. Looking at the differences of nE to sE and eE (Fig. 3 b), lower ET values were found for eroded soils on most days, with some exceptions: i) for rapeseed, few days with higher ET for sE and eE mainly during the fallow period, ii) for winter wheat, a short period with higher ET for sE mainly during the spring period.

2.3 Stable water isotopes

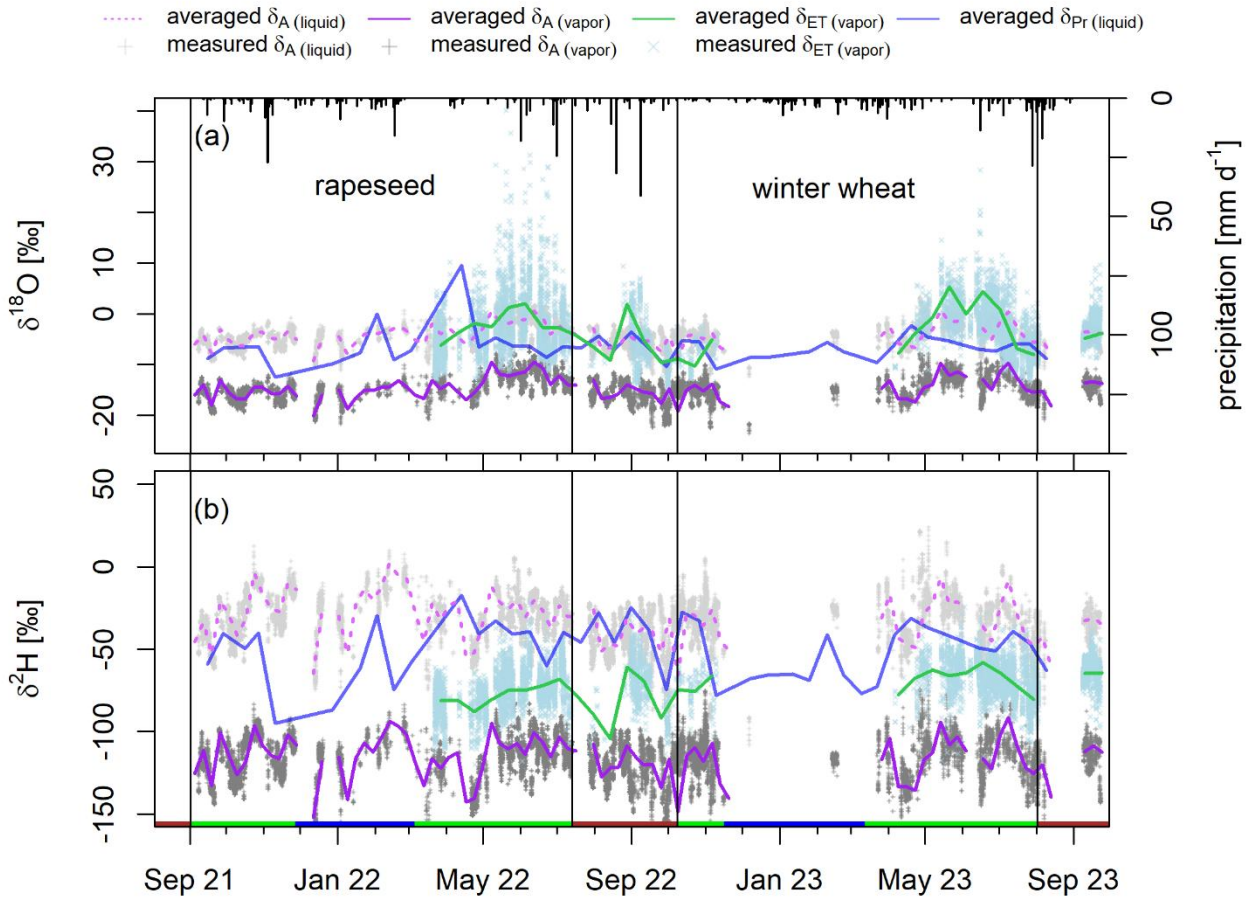


Fig. 4: Stable water isotope overview. The precipitation is illustrated as δ_{Pr} (blue line) and mm d^{-1} (blue bars), the atmospheric water as δ_A in the calculated liquid phase (light grey dots and weekly averages as solid magenta line) and in the measured vapor phase (dark grey dots and weekly averages as dotted purple line), and the ET composition as δ_{ET} in the vapor phase (light blue dots and weekly averages as solid green line). Vertical lines indicate the change of seasons and color of the x-axis denotes different periods during the year with: green for growth, brown for fallow land, and blue for winter

Figure 4 shows the two year timeseries of stable water isotopes in evapotranspiration (light blue dots and green line), ambient water vapor (gray dots and purple/magenta line) and precipitation (blue line). We express the isotopic signatures of both atmospheric vapor (as measured) in addition to predictions of the equilibrated liquid phase; the liquid-phase predictions allow for a more direct comparison with isotopic signatures of precipitation to test the degree of equilibration. In the liquid phase, it is clearly visible that δ_{Pr} and δ_A are predominantly in equilibrium during wet periods such as the beginning of the cultivation periods or in the fallow period of 2022. In contrast, during both main growing periods, δ_A is remarkably in disequilibrium with clearly more heavily enriched values compared to δ_{Pr}. When we look at the vapor phase, the disequilibrium of δ_A can be assigned to the development of δ_{ET} values with highest impact in periods of high ET rates, peaking in May and the beginning of June 2022, or May and June 2023.

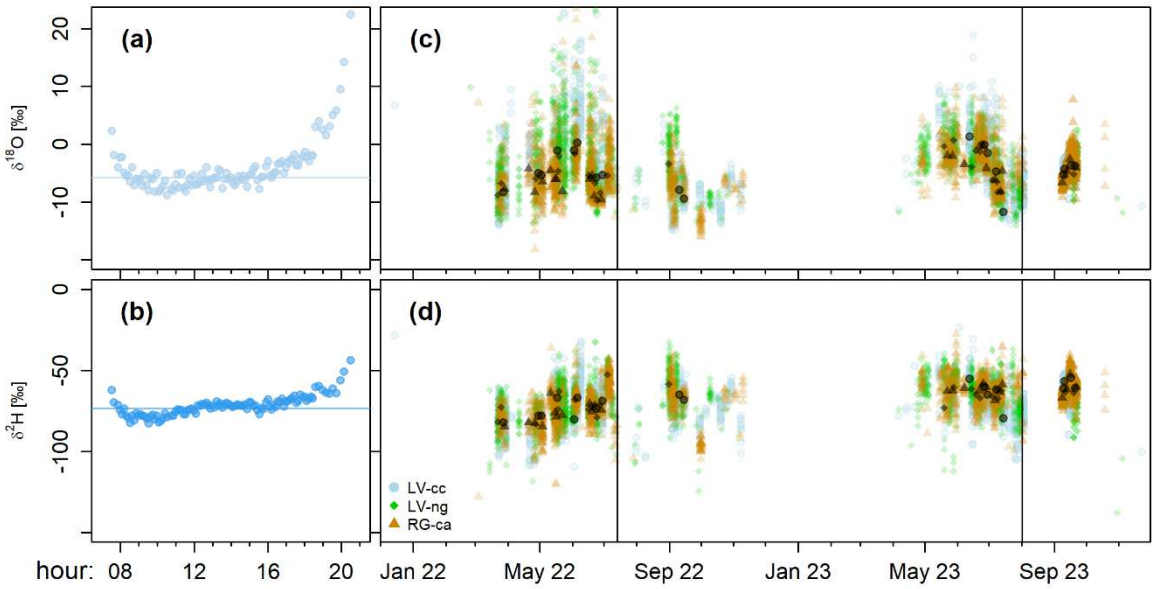


Fig. 5: Results for δ_{ET} using the Keeling-Plot approach. Example of diurnal development of δ_{ET} and isotopic steady-state (a: $\delta^{18}O$ and b: $\delta^{2}H$) for the day with most measurements (June 23rd, 2022) and δ_{ET} over the two cultivation periods (c and d) for the non-eroded LV-cc (green/circles), strongly eroded LV-ng (blue/diamonds) and extremely eroded RG-ca (brown/triangle). The black shapes represent the steady-state values of the corresponding soil type, black horizontal lines the harvest.

Looking at the δ_{ET} values in detail, 6968 values could be created using the Keeling-Plot approach (non-eroded LV-cc = 2215, strongly eroded LV-ng = 2286 and extremely eroded RG-ca = 2467). The mean extrapolation uncertainty after bootstrapping (n = 1000) was found to be +1.33 to -1.22 in $\delta^{18}O$ [‰] and +3.21 to -2.87 in $\delta^{2}H$ [‰]. The high diurnal scatter results mainly from high variations in the morning and evening hours (Fig. 5 a/b). As expected, an isotopic steady state, i.e. δ_{ET} approaching δ_X or isotopic signatures of source water for plant transpiration, was usually reached between 12 and 5 p.m., depending on the time of year and the stability of environmental conditions. Here, periods of stable values highly indicate isotopic steady state. This steady state was determined for each day that had sufficient data available (Fig. 5 b/c black symbols), yielding 19 days for the non-eroded, 25 days for strongly eroded and 25 days for extremely eroded soil. Due to the system's setup to measure only one soil type per day at a high frequency, it was not possible to compare stable water isotopes daily. When we look at the trend over the season (Fig. 5), similar patterns are visible with δ_{ET} values becoming more enriched in heavy isotopes during the main growing seasons followed by a sharp decline to more depleted δ_{ET} values after harvest (c/d). This trend is clearly less visible for the first cultivation period of rapeseed compared to the second cultivation period of winter wheat, which can be explained with the differences in plant development.

2.4 Isoforcing

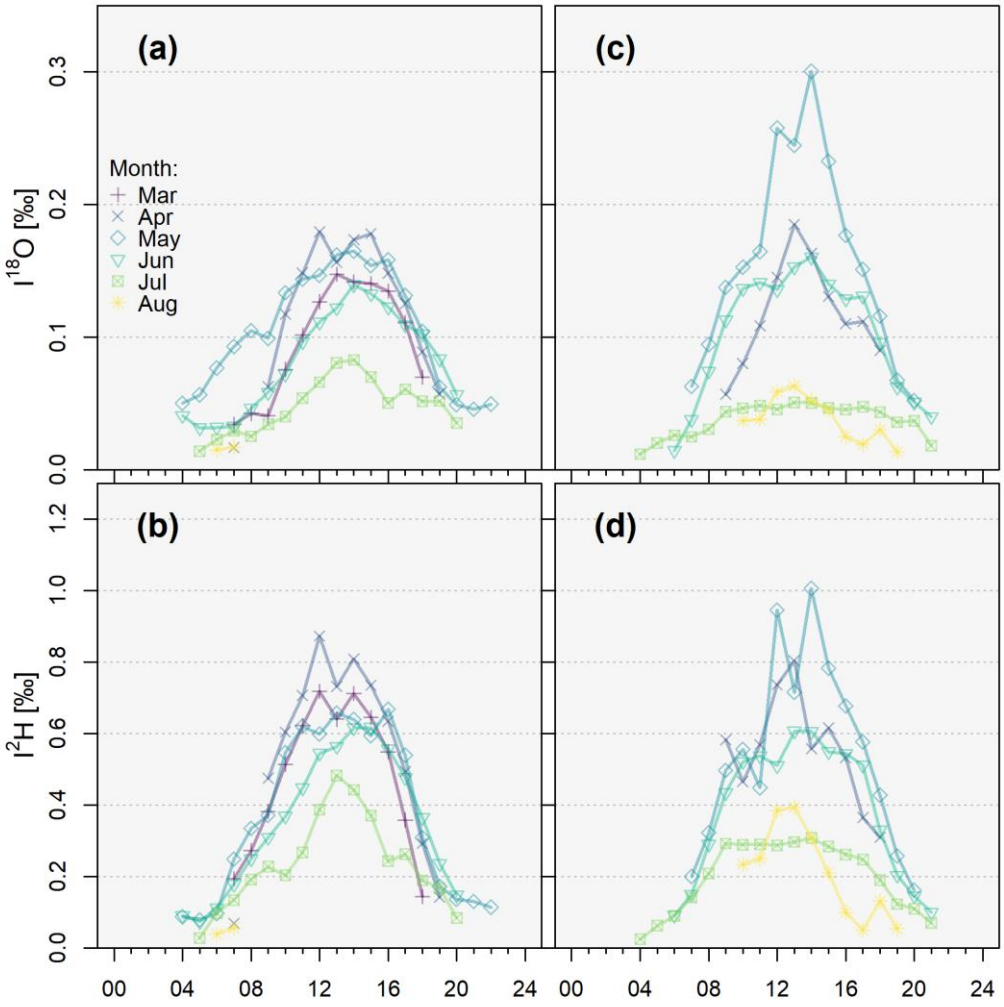


Fig. 6: Isoforcing. Mean hourly isoforcing per month (a/b: $I^{18}O$ and c/d: $I^{2}H$) for the main growing season of 2022 (a/c) and 2023 (b/d), indicated by the point shapes and colors.

Furthermore, we quantify the isoforcing of ET (I_{ET}) on ambient water vapor for $\delta^{18}O$ and $\delta^{2}H$ over both main growing seasons (Fig. 6). Isoforcing quantifies the feedback of the surface water flux on the atmosphere, identifying periods when ET actively alters the isotopic composition of the ambient water vapor. In general, the ratio of evapotranspiration to atmospheric water (ET/w_a) acts as the primary driving factor for isoforcing changes. The data indicate that isoforcing follows the development of ET on the diurnal and seasonal scales. It is striking that high values predominantly occur during the beginning and main period of the growing season for both 2022 and 2023 (roughly June, see Fig S1-S4, supplement). Although relatively high daily ET values still occur during and after ripening, the isoforcing decreases as crops dry.

2.5 Machine learning based isotope modeling

To test and evaluate possible predictive parameters for modeling of δ_{ET}, the Self-Organizing Maps with Sammon's Mapping (SOM-SM) revealed the best parameter combination for both seasons separately being the isotopic composition of ambient water vapor (δ_A), relative humidity (RH), temperature (T), day of the experiment (DOE) and ambient water vapor concentration (C_A) with an r^2-value < 0.85. The presented map sections (Fig. 7) visualize the measured δ_{ET} samples in the SOM-SM. Here, vertical patterns are found for all parameters in various expressions indicating the possibility to be used as modeling parameters. Here, we could not find differences between the different eroded soil types. The distinct pattern of DOE as a seasonal parameter underscores its importance (DOE > RH > T = C_A > δ_A). However, our analysis revealed that models lacking the remaining parameters and especially δ_A failed to accurately simulate δ_{ET}.

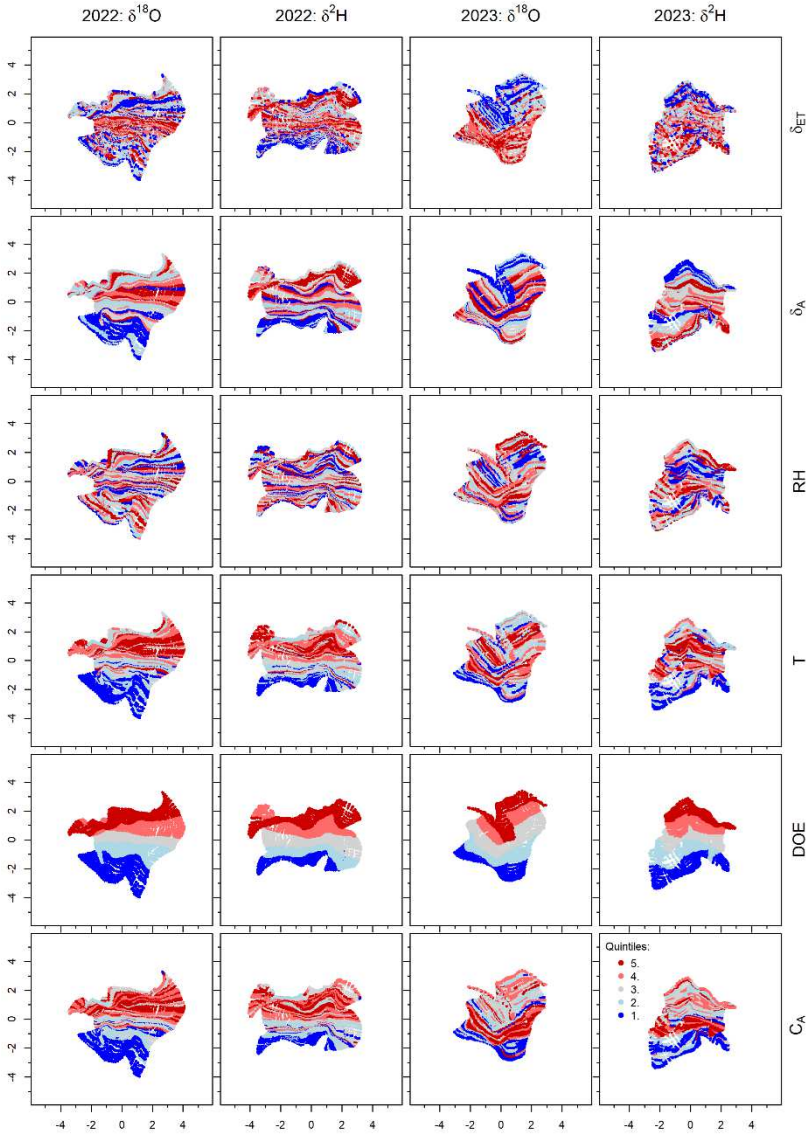


Fig. 7: Self-Organizing Maps with Sammon's Mapping (SOM-SM). Values of the observed samples depicted in the SOM-SM. The first to fifth quintile are illustrated by color (see legend).

Looking at the modeled δ_{ET} values (Fig. 8), the RF prediction revealed a good fit for δ_{ET} for both seasons visible in the comparison between measured and validation data (Fig. 8, right side/e-h; $\delta^{18}O$: MAE < 1.5, NRMSE < 36, KGE > 0.85 and r2 > 0.88; δ^2H: MAE < 3.5, NRMSE < 44, KGE > 0.77 and r2 > 0.8). No clear over- or underestimation was found. Modelling gaps within the period originated from missing δ_A data. During 2022 (Fig. 8 a/c), the model predicted data gaps up to a week with reasonable data compared to directly observed diurnal variations according

to the seasonal period (e.g. mid of June). After harvest in mid-July, no data were available and the predictions were highly questionable. The data availability for the initial period of 2023 (Fig. 8 b/c) from mid- March to the end of April exposed only slight changes over the day and might not have shown the actual dynamics. The following period with better data availability then again indicated diurnal and seasonal dynamics over three months during the main growth period with a slight trend to an enrichment of heavy stable water isotopes during periods of increased ET. A comparison of both seasons revealed an increased magnitude with higher variations for oil rapeseed in the first season than for winter wheat in the second. Consistent with the ET modeling results, the best model performance was achieved when measurements integrated the entire observation period.

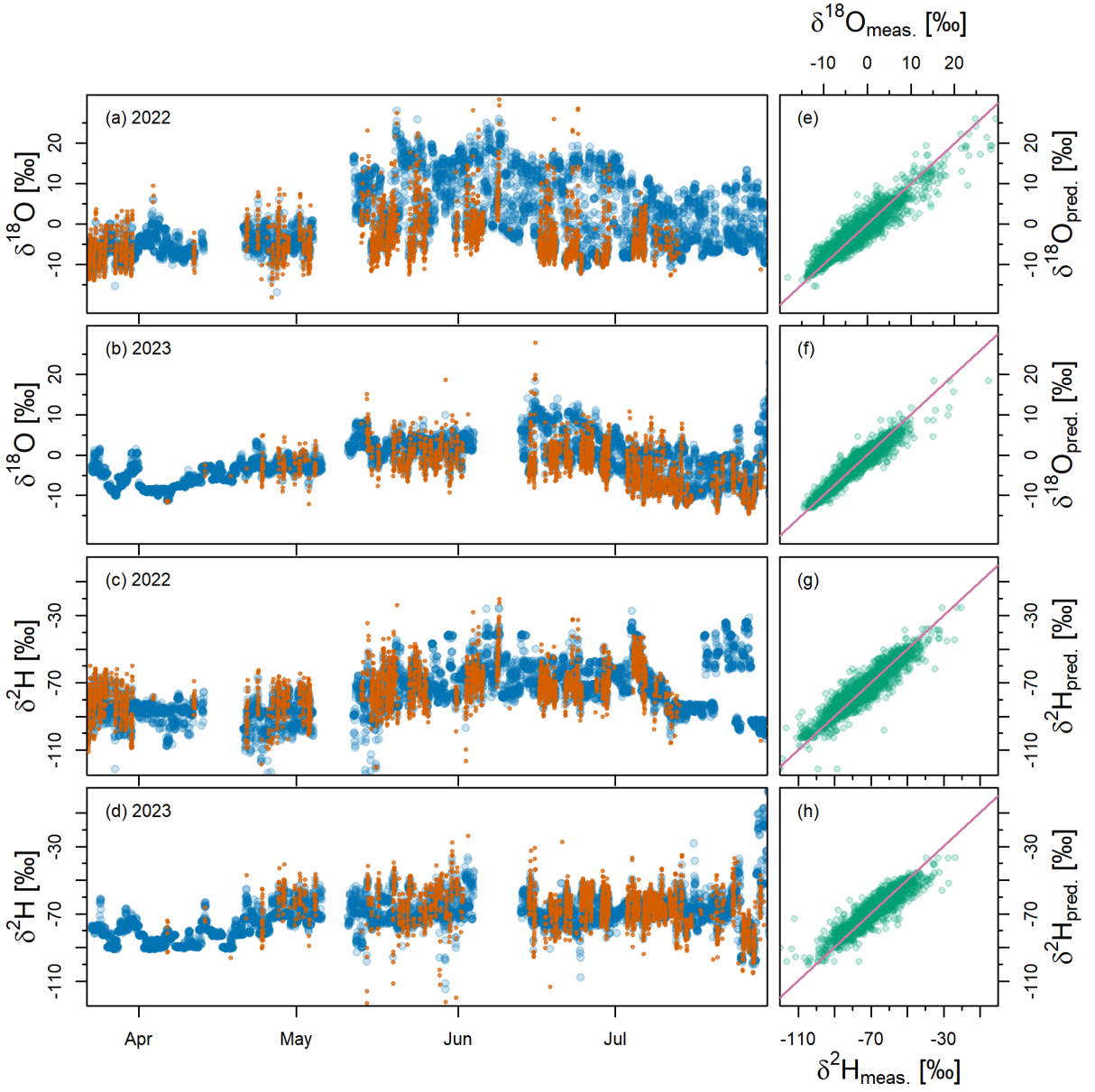


Fig. 8: δ_{ET} modeling. (a)-(d) Estimated δ_{ET} using the Keeling-Plot approach (orange small dots) vs. predicted δ_{ET} using the Random Forest approach (blue dots). (e)-(h) Measured to validated data for both stable water isotopes (green dots; $\delta^{18}O$ and $\delta^{2}H$) with a 1-1 line (pink).

3. Discussion

By combining high-resolution ET and in-situ stable water isotope monitoring ($\delta^{18}O$ and $\delta^{2}H$) with machine learning approaches, we addressed two hypotheses: First, we demonstrated how δ_{ET} serves as a sensitive indicator for the physiological response of crop systems (oil rapeseed and winter wheat) to water availability and phenological stages, revealing non-steady-state patterns often missed by lower-resolution methods. Second, the results confirm that strong ET fluxes apply measurable isoforcing on the ambient water vapor within the lower atmospheric boundary layer (δ_A), challenging the common assumption of isotopic equilibrium between precipitation (δ_{Pr}) and δ_A. Furthermore, we showed that machine learning models (Random Forest) can effectively predict high-frequency δ_{ET} dynamics from common micrometeorological variables and the simple measurable ambient water vapor δ_A, providing a robust alternative to computationally expensive physical models for gap-filling.

The observed progressive enrichment of δ_{ET} throughout the growing season is likely driven by a mixture of three concurrent mechanisms: (1) the phenological shift in the ET fluxes (T/ET ratio), (2) the evaporative enrichment of the soil water source and (3) the incoming precipitation. During early growth or fallow periods, soil evaporation (E) dominates ET, releasing vapor strongly depleted in heavy isotopes via kinetic fractionation[5,13]. As the crop canopy develops, the contribution of transpiration (T) increases (1) and shifts δ_{ET} towards more enriched values relative to soil evaporation[15,24]. Contrasting this biological control is the abiotic development of the soil water source. Short summer drought (e.g., May/June 2023) likely drove strong evaporative enrichment (2) in the upper soil layers[32,40]. Consequently, E and shallow root water uptake draw from this pool, further enriching δ_{ET}[41]. Additionally, higher temperatures during growth elevate the isotopic baseline with more enriched precipitation (3) compared to winter precipitation[25,26]. Therefore, the observed seasonal δ_{ET} enrichment reflects a transition from evaporation-dominated depleted winter to a transpiration-dominated enriched summer, amplified by evaporative enrichment during droughts.

Diurnally, while the simplified Craig-Gordon approach assuming isotopic steady-state (ISS) between δ_T and δ_A can be inaccurate[13], our high-resolution measurements indicate ISS conditions for most daytime periods (69 d). This aligns with the species-specific leaf water turnover time (τ), which describes the required time to reach isotopic steady state, largely controlled by stomatal conductance (g_s) and leaf water volume (W)[35,42,43]. Our data revealed

that winter wheat likely exhibits a shorter τ due to a lower leaf water volume and consequently reaches ISS faster. Winter wheat exhibits a smaller diurnal magnitude of isotopic deviation from the source water compared to rapeseed. Typically, rapeseed maintains significantly higher stomatal conductance compared to winter wheat, but it becomes heavily conservative under limited water conditions [44,45]. This regulation emphasizes shorter non-steady state (NSS) periods for crops with slower turnover times, whereas crops with fast turnover times like winter wheat may operate near ISS for extended periods.

Beyond the dynamics between ET and ambient water vapor, we want to highlight the isotopic relationship between precipitation and ambient water vapor (δ_A). Our two-week bulk precipitation samples (δ_{Pr}) indicate a disequilibrium between δ_A and δ_{Pr} during the main growing periods with high ET fluxes. Specifically, in the absence of direct measurements, models often rely on the assumption that δ_A is in isotopic equilibrium with recent precipitation[10,46,47]. This equilibrium assumption has been used to estimate the isotopic composition of δ_A from δ_{Pr}[10,48], e.g. in models like the EcH$_2$O-iso[49]. Our high-resolution observations confirm recent findings that this equilibrium assumption is frequently violated, particularly during periods of high transpiration and convective precipitation[20,50–53]. Therefore, explicit monitoring of δ_A is essential, as relying on equilibrium-based estimates derived from δ_{Pr} would distort the atmospheric boundary conditions in ecohydrological models.

Isoforcing (I_{ET}) quantifies the impact of the ET flux on the isotopic composition of the ambient water vapor in the lower atmospheric boundary layer[12,54]. Our data reveals that the ratio of ET to atmospheric water concentration (ET/w_a) acts as the primary driving factor. Consequently, we observed peak I_{ET} values both at the beginning of the growing season, driven abiotical by a dry atmosphere (low w_a), and during the main vegetation period, driven biotical by high transpiration rates (high ET). The high impact of vegetation on the isotopic composition of water vapor leads to disequilibrium between the isotopic composition of atmospheric vapor (δ_A) and precipitation (δ_{Pr}).

With rising computational power and development of machine learning, the number of studies using data-driven modeling approaches has increased rapidly. They have been used in isotope hydrology to estimate stream and groundwater concentrations[55] or predict rainfall isotopic values[56], to map ecohydrological Isoscapes[57] or to model global plant transpiration[58]. While previous studies have often relied on lower-frequency data, recent work demonstrates that sub-

daily dynamics of stable water isotopes are essential to capture rapid changes in vegetation-mediated water cycling[23]. To the best of our knowledge, data driven modeling of stable water isotopes (especially δ_{ET}) over one or more whole growing seasons has not been achieved previously. The SOM-SM concept used here to evaluate important drivers[59,60] enabled us to find and evaluate possible predictors for δ_{ET} (DOE > RH > T = C_A > δ_A). While long periods of insufficient data, especially at the beginning and end of the period of consideration, revealed high uncertainty, the main growing periods with good data availability resulted in promising results. Based on our findings, we assume that the integration of daily precipitation isotope data combined with high-resolution δ_A measurements could substantially improve the performance of process-based ecohydrological models, such as EcH2O-iso[27]. Consequently, we suggest that high-resolution δ_A data may serve as a more robust and accessible constraint for modeling ET partitioning than plant tissue isotopes, which are labor-intensive, destructive, and often subject to extraction artifacts[11,23]. This is supported by Birkel *et al.*[50], who showed that atmospheric vapor isotopes integrate ecohydrological fluxes and can constrain model equifinality better than xylem data, which often exhibit unexplained high-frequency variability. Additionally, the continuous monitoring of microclimate, precipitation, δ_{Pr} and δ_A proved to be much easier to implement and maintain than continuous xylem monitoring, yet it explained variations in δ_{ET} sufficiently well. However, we assume that, similar to ET modeling, the variability of the data is crucial for the model[7] and that high-resolution δ_{Pr} values could significantly improve the modeling.

This study used a fully automated, closed chamber system (FluxCrane) combined with in situ measurements of stable water isotopes to investigate the complex dynamics of the soil-plant-atmosphere continuum (SPAC) over two growing seasons. The connection of continuous, high-resolution measurements with isoforcing enabled to better explain short-term variations and seasonal dynamics that cannot be achieved by manual or destructive methods. On the diurnal scale, the results support the finding that simplified approaches to modeling δ_T assuming an isotopic steady state (ISS) may be inaccurate. On the seasonal scale, regarding the feedback between the land surface and the atmosphere, we show that the crop canopy exerts a strong isoforcing on ambient water vapor in the atmospheric boundary layer during periods of high physiological activity. This biotic forcing drives atmospheric water vapor away from isotopic equilibrium with precipitation, thereby challenging the validity of the equilibrium assumption frequently applied in classical ecohydrological models. Consequently, our findings highlight that

explicit monitoring of ambient water vapor isotopes (δ_A) is essential. These findings were complemented by the first successful validation of data-driven Random Forest (RF) modeling supported by SOM-SM to predict high-frequency δ_{ET} dynamics using standard micrometeorological variables and δ_A. The RF approach provided promising results for half-hourly prediction of δ_{ET} during the main growing seasons. Coupling such high-resolution plot data with machine learning approaches offers a promising pathway for upscaling and validating field-scale fluxes[7,39]. However, future applications must critically assess the trade-offs regarding data quantity versus quality, particularly the impact of observation gaps during the non-growing season and the need for increased temporal resolution of precipitation sampling.

4. Methods

4.1 Field site and cultivation

The field experiments took place at the AgroFlux experimental platform of ZALF (see Dahlmann *et al.*[7] or Hoffmann *et al.*[61] for further details), located in the northeast of Germany, near Dedelow in the Uckermark region (N 53°22′45", E 13°47′11"; ~50-60 m a.s.l.). The site is located in the continental climate zone with a long-term (1991 to 2020; ZALF) annual mean air temperature of 8.8 °C and an annual mean precipitation of 467 mm (ZALF research station, Dedelow). The experiments were conducted on two identical fields, each measuring 100 by 16 meters. The study site exhibits three distinct soil types that represent local erosion stages: non-eroded Calcic Luvisol (LV-cc), strongly eroded Nudiargic Luvisol (LV-ng), and extremely eroded Calcaric Regosol (RG-ca)[62]. More detailed information on these soil types is available in Sommer *et al.*[63]. The measurements were performed from September 2021 until end of August 2023 with cultivation of rapeseed (*Brassica napus L.,* 1st September 2021- 13th July 2022) and winter wheat (*Triticum aestivum,* 8th October 2022 - 1st August 2023). The start and end of the cultivation periods were defined as germination and harvest.

4.2 Experimental design

Measurements were performed a) using the fully automated gantry crane system FluxCrane and b) the reference field next to it for destructive measurements. The 5-meter-high FluxCrane, described in detail by Dahlmann *et al.*[7], is a system designed for automatic three-dimensional sampling (Pfannenstiel ProProject GmbH, Bad Tölz, Germany). It moves along the x-axis, perpendicular to the tracks along the y-axis, and vertically along the z-axis to deploy chambers for measurements throughout the entire field. The FluxCrane carries two transparent polymethyl methacrylate (PMMA) chambers (Area: 1.986 m^2; Volume: 3.756 m^3). To ensure an airtight seal during deployment, steel frames (5 cm depth) with foam rings were installed at all possible sampling plots.

We established a total of 36 plots, with 12 plots dedicated to each soil type. Each set of 12 plots per soil type was subjected to a randomized, full-factorial design. Since only one CRDS was available, the stable water isotopes (δ^2H and $\delta^{18}O$) were measured in only one chamber, with six plots per soil type, for a total of 18 plots. The treatments included two fertilizer types (organic and mineral) applied to six plots each. Additionally, six plots underwent topsoil dilution by incorporating subsoil and decreasing the SOC content to simulate increased erosion, resulting

in four distinct treatment combinations per soil type. Based on previous experiments that showed no significant differences in water fluxes between fertilizer and topsoil dilution, this study focused solely on comparing the three soil types. Possible treatment differences were still tested.

The system measured plots hourly, up to 24 times per day, to capture diurnal variations. The randomized measurement design resulted in each plot being measured approximately twice per week. To secure the system from damage, the system was shut down during high wind velocities and cold temperatures.

To ensure accurate and consistent measurements, the chamber environment was carefully controlled. The chambers have an average light transmittance of approximately 76%. To minimize any potential reduction in plant activity due to chamber closure, the experiment was designed with i) ventilation by two small axial-flow fans (5.61 m^3/min) that homogenized the chamber headspace air, ii) short closing times and iii) carefully selected settings for ET calculations [7]. To compensate for the difference in tubing length between the two chambers and the analyzer (15 m for chamber 1 and 22 m for chamber 2), flow rates were adjusted to 2.3 and 3.6 L/min, respectively, to achieve a consistent sensor dead time of 13s. The similarly cultivated reference field b), which covered the same three soil types, was used for the installation of soil sensors (e.g. for soil water potential (SWP) or measurements up to 150 cm depth).

4.3 Environmental and plant specific parameters

Various environmental and plant specific parameters were measured during the experiment on the FluxCrane and on each treatment or on the reference field (Table 1). Daily ratio vegetation index (RVI) data were estimated from weekly measurements to account for different growth stages. To align the RVI with the other parameters at the half-hourly scale, a sigmoidal function was fitted for the initial plant growth in the fall, while a polynomial function was used for shoot elongation and senescence during spring and summer, respectively. During winter (November 27, 2021, to March 5, 2022, and November 16, 2022, to March 12, 2023), when average daily temperatures were consistently below 5°C, no plant growth was assumed. The yellow rapeseed blossoms posed a challenge for RVI measurements, resulting in increased scatter during the flowering period. Considering this uncertainty and the typical loss of leaves during flowering

(which is usually compensated for by the growth of green pods), a stable RVI value was assumed during this period.

Table 1: Environmental and plant specific parameters

Parameter	Unit	Place	Device
Photosynthetically Active Radiation	$\mu mol\, m^{-2} s^{-1}$	FC, Ch	SKP 215; Skye Instruments Ltd., UK
Air Temperature	°C	FC, Ch	109, Campbell Scientific Ltd., USA
Precipitation	mm	FC, AF	WXT520, Vaisala, FI; Tipping Bucket Rain Gauge 52203; R. M. Young Company, USA
Soil Moisture (5 cm)	%	Tr	ML2x, Delta-T Devices Ltd., UK
Ratio Vegetation Index	-	Tr	SKP 215; Skye Instruments Ltd., UK
Soil Water Potential (5, 15, 45, 150 cm)	kPa	Ref	Teros 21; Meter Group, USA
Windspeed (2 m)	$m\ s^{-1}$	FC	WXT520, Vaisala, FI
Air pressure	hPa	FC	WXT520, Vaisala, FI
Ambient Water Vapor Concentration (C_A)	ppm		Calculated

The ambient water vapor concentration (C_A, in ppm) was derived from measured air temperature (T, in °C), relative humidity (RH, in %), and atmospheric pressure (P, in hPa). First, the saturation vapor pressure (P_s, in Pa) was calculated using the Magnus-Tetens equation[64] (Eq. 1):

$$P_s = 610.78 \times exp\left(\frac{17.2694 \times T}{(T + 238.3)}\right) \quad (1)$$

The actual water vapor partial pressure (p_a, in Pa) was then determined as:

$$p_a = P_s \times \left(\frac{RH}{100}\right) \quad (2)$$

Finally, the water vapor concentration C_A in parts per million (ppm) was calculated by applying Dalton's Law of Partial Pressures, representing the mole fraction of water vapor relative to total atmospheric pressure:

$$C_A = 10^6 \times \left(\frac{p_a}{P}\right) \quad (3)$$

4.4 ET Flux: measurements, calculations and modeling

Evapotranspiration (ET) fluxes were determined in a flow-through non-steady-state (FT-NSS) mode[65] by measuring the development of chamber headspace H_2O concentrations over seven minutes at a 4-second frequency. This was accomplished using LI-COR 850 infrared gas analyzers (LI-COR Biosciences, UK) for each chamber. A CR6 data logger and a CDM-A116 analog multiplexer (Campbell Scientific, Inc., USA) were used for data recording.

The ET fluxes were calculated and processed using the ideal gas equation (Eq. 4/5) modified by Hamel *et al.*[66] coupled with various hard and soft criteria which are described in detail in Dahlmann *et al.*[7]. To reduce the calculation time, the variable moving window size was slightly adjusted to the fixed time of one minute and 20 seconds (20 data points). The fixed window size resulted in considerably faster calculation times without a noticeable change of results.

$$ET_{flux} = \frac{c_{\mathrm{H2O}} \times P \times M_{\mathrm{H2O}}}{R \times T} \times \left(t \times \frac{V}{A}\right) \left[\frac{mm}{d}\right] \quad (4)$$

$$ET_{flux}[mmol\ m^{-2}s^{-1}] = \frac{ET_{flux}\left[\frac{mm}{d}\right]}{(t \times 1000)} * \left(\frac{1}{M_{\mathrm{H2O}}}\right) \quad (5)$$

ET fluxes were modeled on a half-hourly basis following the approach by Dahlmann *et al.*[7] using an RF algorithm (random forest). Following this, the ET budgets for each season were calculated.

4.5 Stable water isotope measurements of ET, ambient water vapor and precipitation

The stable water isotope compositions ($\delta^{18}O$ and $\delta^{2}H$) were measured using a CRDS analyzer in chamber 1 (L2130-i, Picarro Inc., Santa Clara, CA, USA) and are expressed in per mil (‰), relative to the Vienna Standard Mean Ocean Water (VSMOW) using the δ notation[67] (Eq. 6).

$$\delta = \left(\frac{R_{sample}}{R_{VSMOW}} - 1\right) \times 1000[‰] \quad (6)$$

Concentration of ambient water vapor as well as its isotopic composition (δ_A) were estimated at 4 m height above ground (4-2.5 m above canopy depending on plant development). Precipitation samples were taken as two-week bulk samples and analyzed in the laboratory. Weekly averages were calculated for δ_A and δ_{ET}, considering the amount of data per hour to avoid overrepresentation of a specific time of the day. The isotope and gas concentration analyzer was in operation throughout the 2021 -2022 season, while it was removed for maintenance during the winter of the 2022-2023 season.

4.6 Estimation of δ_{ET}: The Keeling-Plot method

The Keeling plot method can be used to disentangle a two-component mixed source like atmospheric CO_2 or H_2O using a linear mass balance framework to estimate the isotopic signature of a specific flux, such as ET[21,33]. The stable water isotopic composition, $\delta^{18}O$ and $\delta^{2}H$, of the variable water source (here ET) can be determined using a linear regression of the isotopic composition against the inverse water vapor concentration (Fig. 9). The y-intercept of this regression represents the variable source's isotopic signature (δ_{ET}).

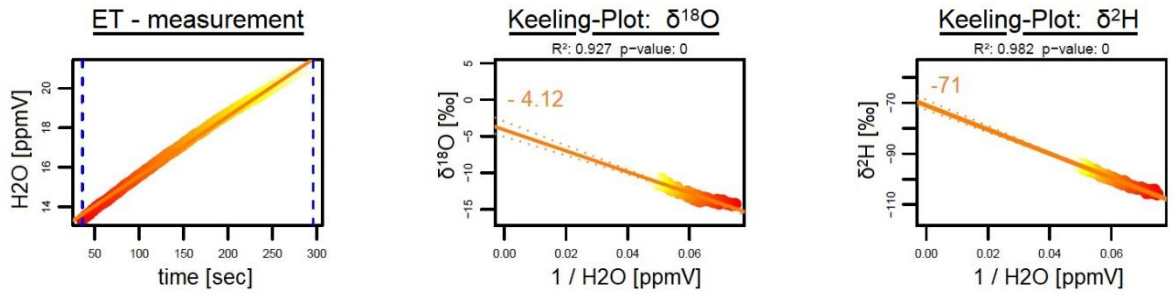


Fig. 9: Example Keeling-Plot. The measurement of the water concentration (x 1000; left), $\delta^{18}O$ (mid), $\delta^{2}H$ (right) and the calculated linear relationship (solid orange line). The uncertainty from bootstrapping is illustrated as dotted line. The color gradient indicates the course of time (red to yellow).

A measurement typically consists of three main stages: 1) a homogenization stage immediately following chamber closure, 2) a sampling stage with a linear relationship of water vapor concentration and stable water isotope readings, and 3) the saturation stage indicated by a decreasing slope of concentration due to a high water concentration within the chamber. To estimate δ_{ET} with the FluxCrane system, the measurements were analyzed using an automated R-script with various tests and selection criteria. The first step was to identify the second stage – the sampling. To do so, subsequent measurements with less than 1000 ppm difference or a negative slope were discarded. Then, a function was applied that removed data points from the beginning or end, depending on the median slope, down to a minimum window size of 45 data points (three minutes), resulting in the longest possible keeling plot within the given criteria for one measurement. Within this function, the measurements were tested for correlation (Pearson correlation; $p < 0.05$), variance (r^2: H2O-concentration > 0.9, $\delta^{18}O$ and $\delta^{2}H > 0.7$) and homoscedasticity (Breusch-Pagan-test; $p < 0.05$). After selecting the keeling plot, the δ_{ET} was determined, and its robustness was tested using bootstrap resampling with 1000 iterations. The period between 11 p.m. and 4 a.m. was excluded due to RH approaching saturation, which resulted in negligible ET.

4.7 Isoforcing

Isoforcing (I_{ET}) quantifies the feedback of the ET flux on ambient water vapor (atmospheric boundary layer) and its isotopic composition. It can be calculated for both $\delta^{18}O$ and $\delta^{2}H$ as follows [12,54]:

$$I_{ET} = \frac{ET}{w_a}(\delta_{ET} - \delta_A) \quad (7)$$

with ET as the measured ET flux in [l m^{-2} s^{-1}], w_a as the calculated atmospheric water concentration in [l m^{-3}], δ_{ET} as the measured isotopic composition of ET and δ_A as the isotopic composition of atmospheric water vapor.

4.8 Self-Organizing Maps with Sammon's Mapping and δ_{ET} Modeling

Self-organizing maps have been developed and combined with Sammon's mapping for a variety of applications[68,69](see Lischeid *et al.*[60] for further details). In our study, we used the r-package "kohonen"[70] to test various parameters and combinations for their ability to model δ_{ET} (Table 2). The analysis has been performed similarly to Lischeid[59] and Lischeid[60] with a rectangular grid of 60 to 45 nodes, up to 1000 iteration steps and the tolerance for stopping being 0.0001. The best combination of parameters was then used to model δ_{ET} on a half-hourly basis for the main growing period of 2022 and 2023 for both ^{18}O or ^{2}H, as well as the whole observed period. Similar to the ET modeling, the data-driven machine learning RF approach was used and compared for modeling of δ_{ET}[7].

Table 2: Tested modeling parameters.

Parameter
δ_{ET} (^{18}O or ^{2}H)
δ_A (^{18}O or ^{2}H)
Photosynthetically Active Radiation (PAR)
Relative Humidity (RH)
Air Temperature (T)
Vapor Pressure Deficit (VPD)
Soil Moisture (SM)
Ratio Vegetation Index (RVI)
Day of Experiment (DOE)
Ambient Water Vapor Concentration (C_A)

5. Data availability

The data will be available upon publication (BonaRes repository).

6. Acknowledgement

The authors wish to acknowledge the Experimental Infrastructure Platform (EIP) of ZALF and Linda Röderer for assisting with the field experiments.

7. Author contribution

AD and MD designed the study. AD conducted experiments and analyzed the data. JM, DD, GL and MH provided support for the experimental setup and analysis methods. AD prepared the paper with supervision from MD and GL as well as contributions from all co-authors.

8. Competing interests

The authors declare no competing interests.

9. Financial support

This research was supported by the Leibniz Centre for Agricultural Landscape Research (ZALF), the Leibniz Association (ISO-SCALE project; grant no. K444/2022), and the German Research Foundation (DFG) through the Research Unit Formula (FOR5664; grant no. 517723694; subprojects 1/2)

10. References

1. Pereira, L. S., Allen, R. G., Smith, M. & Raes, D. Crop evapotranspiration estimation with FAO56: Past and future. *Agric. Water Manag.* **147**, 4–20 (2015).
2. Fisher, J. B. *et al.* The future of evapotranspiration: Global requirements for ecosystem functioning, carbon and climate feedbacks, agricultural management, and water resources. *Water Resour. Res.* **53**, 2618–2626 (2017).
3. Rana, G. & Katerji, N. Measurement and estimation of actual evapotranspiration in the field under Mediterranean climate: a review. *Eur. J. Agron.* **13**, 125–153 (2000).
4. Baldocchi, D. D. Assessing the eddy covariance technique for evaluating carbon dioxide exchange rates of ecosystems: past, present and future. *Glob. Change Biol.* **9**, 479–492 (2003).
5. Kool, D. *et al.* A review of approaches for evapotranspiration partitioning. *Agric. For. Meteorol.* **184**, 56–70 (2014).
6. Pape, L. *et al.* An automated dynamic chamber system for surface exchange measurement of non-reactive and reactive trace gases of grassland ecosystems. *Biogeosciences* **6**, 405–429 (2009).

7. Dahlmann, A. *et al.* Benefits of a robotic chamber system for determining evapotranspiration in an erosion-affected, heterogeneous cropland. *Hydrol. Earth Syst. Sci.* **27**, 3851–3873 (2023).
8. Grossiord, C. *et al.* Plant responses to rising vapor pressure deficit. *New Phytol.* **226**, 1550–1566 (2020).
9. *Hydrologie*. (UTB, Stuttgart, 2026).
10. Gat, J. R. OXYGEN AND HYDROGEN ISOTOPES IN THE HYDROLOGIC CYCLE. *Annu. Rev. Earth Planet. Sci.* **24**, 225–262 (1996).
11. Beyer, M., Kühnhammer, K. & Dubbert, M. In situ measurements of soil and plant water isotopes: a review of approaches, practical considerations and a vision for the future. *Hydrol. Earth Syst. Sci.* **24**, 4413–4440 (2020).
12. Dubbert, M., Cuntz, M., Piayda, A. & Werner, C. Oxygen isotope signatures of transpired water vapor: the role of isotopic non-steady-state transpiration under natural conditions. *New Phytol.* **203**, 1242–1252 (2014).
13. Dubbert, M., Cuntz, M., Piayda, A., Maguás, C. & Werner, C. Partitioning evapotranspiration – Testing the Craig and Gordon model with field measurements of oxygen isotope ratios of evaporative fluxes. *J. Hydrol.* **496**, 142–153 (2013).
14. Dubbert, M., Couvreur, V., Kübert, A. & Werner, C. Plant water uptake modelling: added value of cross-disciplinary approaches. *Plant Biol.* **25**, 32–42 (2023).
15. Dubbert, M. *et al.* Stable oxygen isotope and flux partitioning demonstrates understory of an oak savanna contributes up to half of ecosystem carbon and water exchange. *Front. Plant Sci.* **5**, (2014).
16. Kübert, A. *et al.* Water Stable Isotopes in Ecohydrological Field Research: Comparison Between In Situ and Destructive Monitoring Methods to Determine Soil Water Isotopic Signatures. *Front. Plant Sci.* **11**, 387 (2020).
17. Kübert, A. *et al.* Combined experimental drought and nitrogen loading: the role of species-dependent leaf level control of carbon and water exchange in a temperate grassland. *Plant Biol.* **23**, 427–437 (2021).

18. Kühnhammer, K. *et al.* Continuous in situ measurements of water stable isotopes in soils, tree trunk and root xylem: Field approval. *Rapid Commun. Mass Spectrom.* **36**, e9232 (2022).
19. Marshall, J. D., Cuntz, M., Beyer, M., Dubbert, M. & Kuehnhammer, K. Borehole Equilibration: Testing a New Method to Monitor the Isotopic Composition of Tree Xylem Water in situ. *Front. Plant Sci.* **11**, 358 (2020).
20. Ring, A., Tetzlaff, D., Dubbert, M., Dubbert, D. & Soulsby, C. High-resolution in situ stable isotope measurements reveal contrasting atmospheric vapour dynamics above different urban vegetation. *Hydrol. Process.* **37**, e14989 (2023).
21. Rothfuss, Y. *et al.* Reviews and syntheses: Gaining insights into evapotranspiration partitioning with novel isotopic monitoring methods. *Biogeosciences* **18**, 3701–3732 (2021).
22. Volkmann, T. H. M. & Weiler, M. Continual in situ monitoring of pore water stable isotopes in the subsurface. *Hydrol. Earth Syst. Sci.* **18**, 1819–1833 (2014).
23. Ring, A.-M., Tetzlaff, D., Birkel, C. & Soulsby, C. Sub-daily stable water isotope dynamics of urban tree xylem water and ambient vapor. *Hydrol. Earth Syst. Sci.* **29**, 6663–6683 (2025).
24. Wang, X.-F. & Yakir, D. Using stable isotopes of water in evapotranspiration studies. *Hydrol. Process.* **14**, 1407–1421 (2000).
25. Gat, J. R. & Airey, P. L. Stable water isotopes in the atmosphere/biosphere/lithosphere interface: Scaling-up from the local to continental scale, under humid and dry conditions. *Glob. Planet. Change* **51**, 25–33 (2006).
26. Zhang, X. *et al.* Simulation of stable water isotopic composition in the atmosphere using an isotopic Atmospheric Water Balance Model. *Int. J. Climatol.* **35**, 846–859 (2015).
27. Kuppel, S., Tetzlaff, D., Maneta, M. P. & Soulsby, C. EcH_2 O-iso 1.0: water isotopes and age tracking in a process-based, distributed ecohydrological model. *Geosci. Model Dev.* **11**, 3045–3069 (2018).
28. Braden-Behrens, J., Markwitz, C. & Knohl, A. Eddy covariance measurements of the dual-isotope composition of evapotranspiration. *Agric. For. Meteorol.* **269–270**, 203–219 (2019).

29. Good, S. P., Soderberg, K., Wang, L. & Caylor, K. K. Uncertainties in the assessment of the isotopic composition of surface fluxes: A direct comparison of techniques using laser-based water vapor isotope analyzers. *J. Geophys. Res. Atmospheres* **117**, 2011JD017168 (2012).
30. Stoy, P. C. *et al.* Reviews and syntheses: Turning the challenges of partitioning ecosystem evaporation and transpiration into opportunities. *Biogeosciences* **16**, 3747–3775 (2019).
31. Cernusak, L. A., Pate, J. S. & Farquhar, G. D. Diurnal variation in the stable isotope composition of water and dry matter in fruiting *Lupinus angustifolius* under field conditions. *Plant Cell Environ.* **25**, 893–907 (2002).
32. Dubbert, M. & Werner, C. Water fluxes mediated by vegetation: emerging isotopic insights at the soil and atmosphere interfaces. *New Phytol.* **221**, 1754–1763 (2019).
33. Keeling, C. D. The concentration and isotopic abundances of atmospheric carbon dioxide in rural areas. *Geochim. Cosmochim. Acta* **13**, 322–334 (1958).
34. Craig, H. & Gordon, L. I. Deuterium and oxygen 18 variations in the ocean and the marine atmosphere. (1965).
35. Dongmann, G., Nürnberg, H. W., Förstel, H. & Wagener, K. On the Enrichment of H2180in the Leaves of Transpiring Plants. (1974).
36. Braud, I., Bariac, T., Gaudet, J. P. & Vauclin, M. SiSPAT-Isotope, a coupled heat, water and stable isotope (HDO and H218O) transport model for bare soil. Part I. Model description and first verifications. *J. Hydrol.* **309**, 277–300 (2005).
37. Haverd, V. & Cuntz, M. Soil–Litter–Iso: A one-dimensional model for coupled transport of heat, water and stable isotopes in soil with a litter layer and root extraction. *J. Hydrol.* **388**, 438–455 (2010).
38. Sprenger, M. *et al.* Measuring and Modeling Stable Isotopes of Mobile and Bulk Soil Water. *Vadose Zone J.* **17**, 1–18 (2018).
39. Nelson, J. A. *et al.* Ecosystem transpiration and evaporation: Insights from three water flux partitioning methods across FLUXNET sites. *Glob. Change Biol.* **26**, 6916–6930 (2020).

40. Barnes, C. J. & Allison, G. B. The distribution of deuterium and 18O in dry soils. *J. Hydrol.* **60**, 141–156 (1983).
41. Xu, M. *et al.* Characterization of spatiotemporal patterns of soil water stable isotopes at an agricultural field. *Sci. Total Environ.* **828**, 154538 (2022).
42. Dubbert, M., Kübert, A. & Werner, C. Impact of Leaf Traits on Temporal Dynamics of Transpired Oxygen Isotope Signatures and Its Impact on Atmospheric Vapor. *Front. Plant Sci.* **8**, (2017).
43. Farquhar, G. D. & Cernusak, L. A. On the isotopic composition of leaf water in the non-steady state. *Funct. Plant Biol.* **32**, 293–303 (2005).
44. Farquhar, G. D., Cernusak, L. A. & Barnes, B. Heavy Water Fractionation during Transpiration. *Plant Physiol.* **143**, 11–18 (2007).
45. Hess, L., Meir, P. & Bingham, I. J. Comparative assessment of the sensitivity of oilseed rape and wheat to limited water supply. *Ann. Appl. Biol.* **167**, 102–115 (2015).
46. Gibson, J. J. & Edwards, T. W. D. Regional water balance trends and evaporation-transpiration partitioning from a stable isotope survey of lakes in northern Canada. *Glob. Biogeochem. Cycles* **16**, (2002).
47. Horita, J., Rozanski, K. & Cohen, S. Isotope effects in the evaporation of water: a status report of the Craig–Gordon model. *Isotopes Environ. Health Stud.* **44**, 23–49 (2008).
48. Gibson, J. J. & Reid, R. Water balance along a chain of tundra lakes: A 20-year isotopic perspective. *J. Hydrol.* **519**, 2148–2164 (2014).
49. Chávez-Espinoza, D., Kuppel, S., Peugeot, C., Yoshimura, K. & Vallet-Coulomb, C. Sensitivity of Stable Isotope Dynamics to Parametric and Conceptual Choices in Critical Zone Hydrological Modelling—A Case Study in Tropical Africa. *Hydrol. Process.* **39**, e70337 (2025).
50. Birkel, C., Tetzlaff, D., Ring, A.-M. & Soulsby, C. Does high resolution in situ xylem and atmospheric vapor isotope data help improve modeled estimates of ecohydrological partitioning? *Agric. For. Meteorol.* **365**, 110467 (2025).

51. Mercer, J. J., Liefert, D. T. & Williams, D. G. Atmospheric vapour and precipitation are not in isotopic equilibrium in a continental mountain environment. *Hydrol. Process.* **34**, 3078–3101 (2020).

52. Penchenat, T. *et al.* Isotopic Equilibrium Between Precipitation and Water Vapor in Northern Patagonia and Its Consequences on $\delta^{18}O_{cellulose}$ Estimate. *J. Geophys. Res. Biogeosciences* **125**, e2019JG005418 (2020).

53. Vimeux, F. & Risi, C. Isotopic equilibrium between raindrops and water vapor during the onset and the termination of the 2005–2006 wet season in the Bolivian Andes. *J. Hydrol.* **598**, 126472 (2021).

54. Lee, X. *et al.* Canopy-scale kinetic fractionation of atmospheric carbon dioxide and water vapor isotopes. *Glob. Biogeochem. Cycles* **23**, 2008GB003331 (2009).

55. Sahraei, A., Houska, T. & Breuer, L. Deep Learning for Isotope Hydrology: The Application of Long Short-Term Memory to Estimate High Temporal Resolution of the Stable Isotope Concentrations in Stream and Groundwater. *Front. Water* **3**, 740044 (2021).

56. Maliki, A. A. *et al.* Employing artificial intelligence to predict $\delta^{18}O$ and $\delta^{2}H$ isotope ratios in precipitation in Iraq under changing climate patterns. *Sci. Rep.* **16**, 1296 (2026).

57. Hill, A. F., McKenzie, A., Dudley, B. D. & Nelson, D. B. Precipitation Isotopes New Zealand (PINZ): improvements in precipitation isoscapes with machine learning. *Environ. Chem.* **22**, EN24098 (2025).

58. Hannemann, M., García-García, A., Poyatos, R., Mahecha, M. D. & Peng, J. Estimating transpiration globally by integrating the Priestley-Taylor model with neural networks. *Environ. Res. Lett.* **19**, 114089 (2024).

59. Lischeid, G. Non-linear visualization and analysis of large water quality data sets: a model-free basis for efficient monitoring and risk assessment. *Stoch. Environ. Res. Risk Assess.* **23**, 977–990 (2009).

60. Lischeid, G., Kalettka, T., Merz, C. & Steidl, J. Monitoring the phase space of ecosystems: Concept and examples from the Quillow catchment, Uckermark. *Ecol. Indic.* **65**, 55–65 (2016).

61. Hoffmann, M. *et al.* Advancing sustainable agricultural transformation through the synergy of automated experimental platforms and living labs. *Nat. Commun.* **16**, 8418 (2025).
62. Schad, P. The International Soil Classification System WRB, Third Edition, 2014. in *Novel Methods for Monitoring and Managing Land and Water Resources in Siberia* (eds. Mueller, L., Sheudshen, A. K. & Eulenstein, F.) 563–571 (Springer International Publishing, Cham, 2016). doi:10.1007/978-3-319-24409-9_25.
63. Sommer, M., Gerke, H. H. & Deumlich, D. Modelling soil landscape genesis — A "time split" approach for hummocky agricultural landscapes. *Geoderma* **145**, 480–493 (2008).
64. Murray, F. W. On the computation of saturation vapor pressure. *Journal of Applied Meteorology and Climatology* 203–204 (1967).
65. Livingston, G. P. & Hutchinson, G. L. Enclosure-based measurement of trace gas exchange: applications and sources of error. in *Biogenic Trace Gases: Measuring Emissions from Soil and Water* 14–51 (John Wiley & Sons, Incorporated, Hoboken, 1995).
66. Hamel, P. *et al.* Automated Chamber System to Measure Field Evapotranspiration Rates. *J. Hydrol. Eng.* **20**, 04014037 (2015).
67. Craig, H. Standard for Reporting Concentrations of Deuterium and Oxygen-18 in Natural Waters. *Science* **133**, 1833–1834 (1961).
68. Sammon, J. W. A nonlinear mapping for data structure analysis. I. *IEEE Transactions on computers* 401–409 (1969).
69. Kohonen, T. *Self-Organizing Maps*. (Springer, Berlin Heidelberg, 2001). doi:10.1007/978-3-642-56927-2.
70. Wehrens, R. & Kruisselbrink, J. Flexible Self-Organizing Maps in **kohonen** 3.0. *J. Stat. Softw.* **87**, (2018).

Supplement:

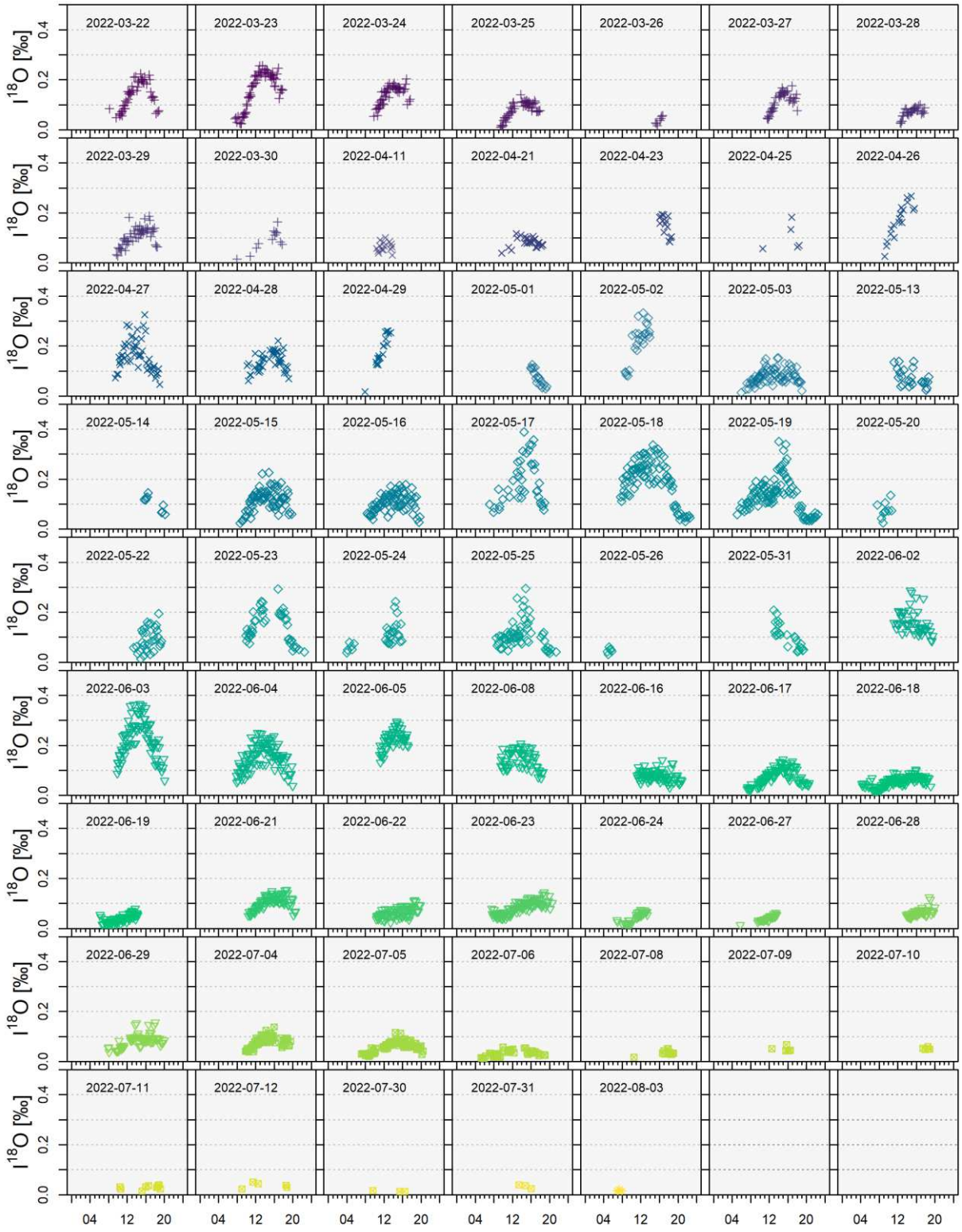


Fig. S1: Diurnal ^{18}O isoforcing ($I^{18}O$) for the growing season of oil rapeseed 2022.

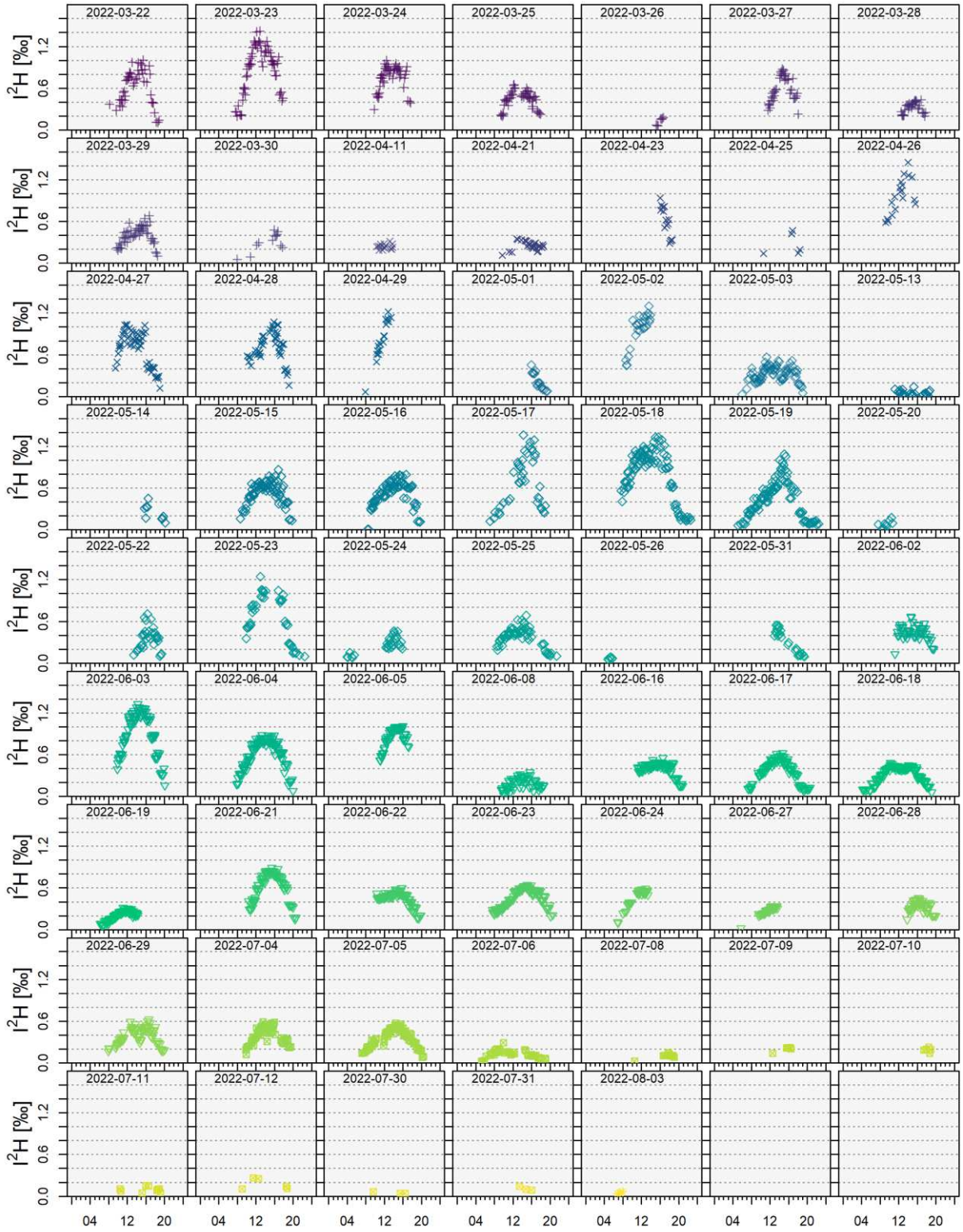


Fig. S2: Diurnal ^2H isoforcing (I^2H) for the growing season of oil rapeseed 2022.

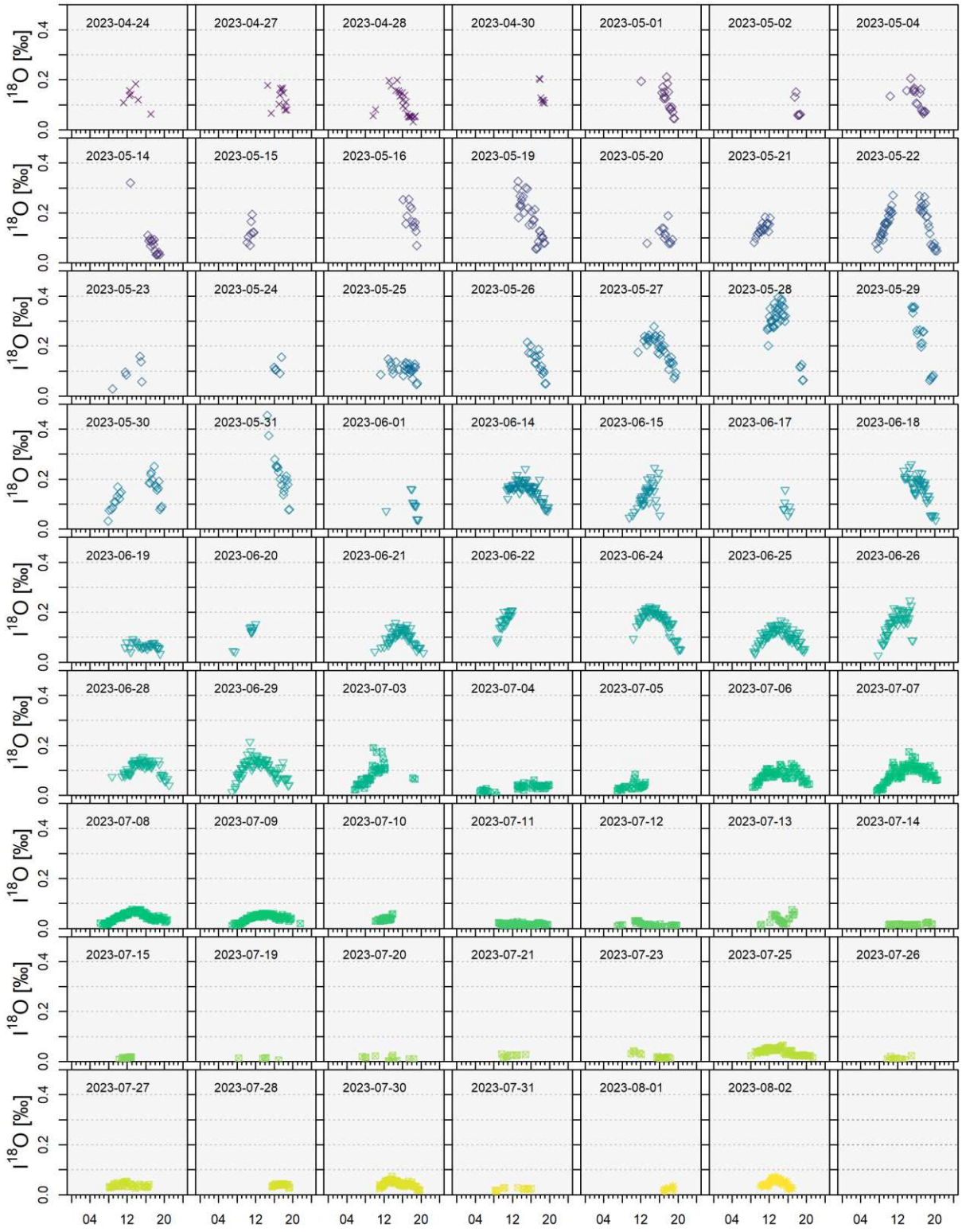


Fig. S3: Diurnal ^{18}O isoforcing ($I^{18}O$) for the growing season of winter wheat 2023.

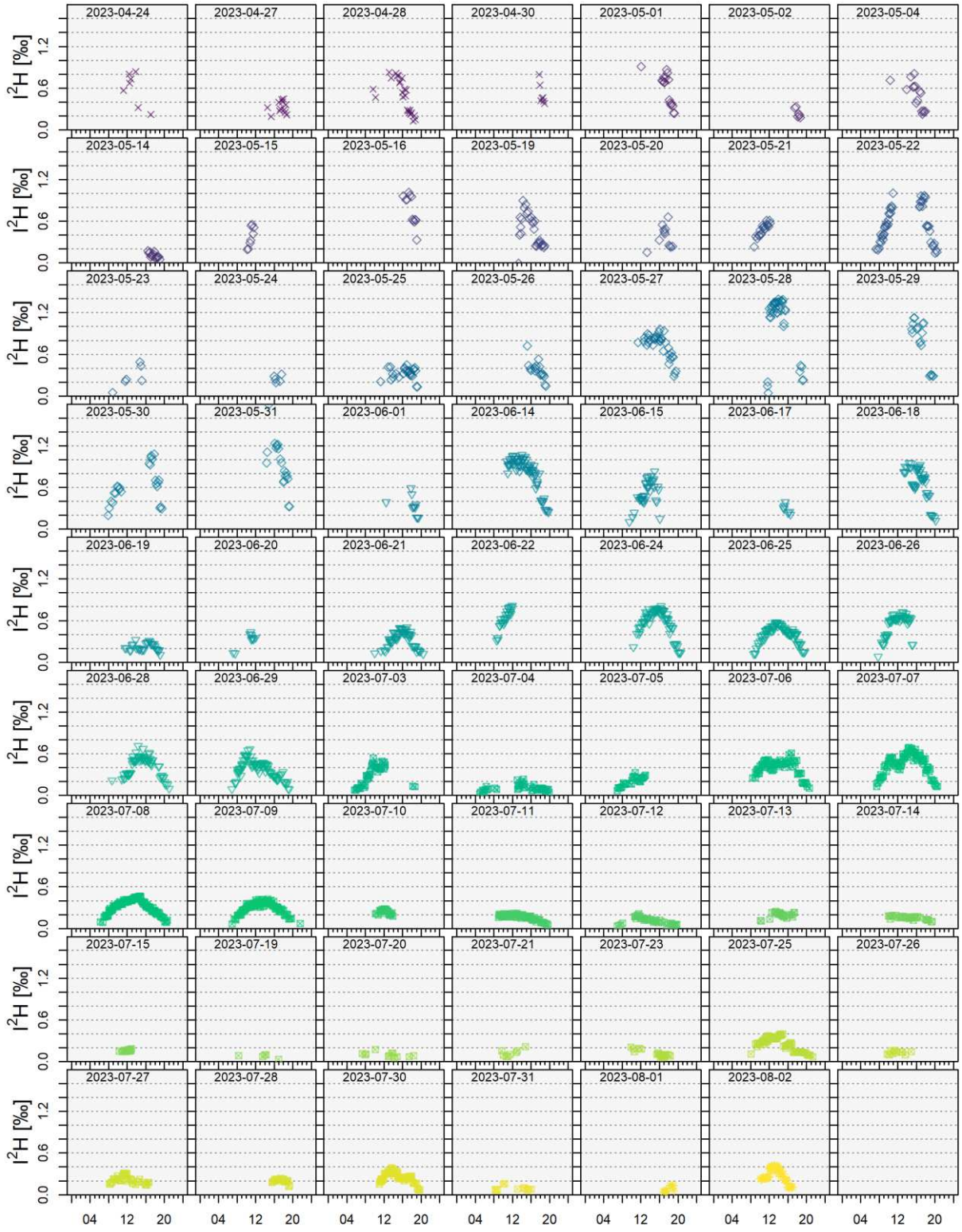


Fig. S4: Diurnal ^2H isoforcing (I^2H) for the growing season of winter wheat 2023.

Supplementary Files

This is a list of supplementary files associated with this preprint. Click to download.

- reportingsummaryNCOMMS26021086.pdf